Interpretation of Scattering Phenomenology in Slotted Waveguide Structures via Time-Frequency Processing

Luiz C. Trintinalia and Hao Ling, *Senior Member, IEEE*

Abstract—The scattering phenomenology in slotted waveguide structures is investigated using time-frequency processing of numerically simulated data. Two geometries are studied, a finite waveguide with one slot on each end and a linear slotted waveguide array comprised of 16 equally spaced slots. The numerical simulation is accomplished via a three-dimensional moment-method procedure in conjunction with a connection scheme which makes possible the simulation of a long waveguide structure spanning over 32 wavelengths at 10 GHz. The resulting numerical data are then processed using the short-time Fourier transform to identify the dominant scattering mechanisms. In the joint time-frequency plane, the unique scattering physics associated with slotted waveguide structures are more clearly revealed. In particular, the Floquet harmonics due to the exterior slot structure, the dispersion due to the interior waveguide modes, and the "interior Floquet" phenomenon can be readily identified and fully interpreted.

I. INTRODUCTION

IT is well recognized by the radar signature community that the scattering from antenna structures can often be the dominant contributor to the overall radar cross section (RCS) of a target platform. To properly account for the antenna RCS, many analysis methodologies based on numerical, asymptotic, and hybrid techniques have been developed to date. Furthermore, to enhance the understanding of the prediction results, a number of post-processing tools are available for interpreting and correlating the resulting signal constituents with the scattering phenomenology of the structure. For example, one-dimensional range profile (or impulse response) and two-dimensional (2–D) inverse synthetic aperture radar (ISAR) imagery are effective means of spatially mapping the point scatterers in the structure. Together, the RCS prediction tools and post-processing algorithms form the basis of what can be termed a signature analysis cycle.

In this paper, we carry out such a two-part study for slotted waveguide structures. Waveguide slot is a commonly found configuration in phased array antennas. Our motivation in this study is to better understand the scattering phenomenology in such structures and to explore the resulting implications for target identification applications. In the first part of this work, the scattering from the waveguide array structure is simulated using a method-of-moments procedure in conjunction with a connection scheme we have developed recently [1], [2]. The connection algorithm allows a large structure to be analyzed in pieces before the analyzed sections are cascaded together. This scheme makes possible the simulation of a 16-element slotted waveguide array which spans over 32 wavelengths in one dimension at the highest frequency of interest. In the second part of this study, we process the resulting numerical data in the joint time-frequency feature space. In contrast to the traditional range profile or ISAR imagery, the joint time-frequency processing was only recently introduced into the electromagnetic scattering community [3]–[13]. It was found that scattering mechanisms, which may not be immediately apparent in the traditional feature spaces, become quite revealing in the joint time-frequency plane. Scattering centers, target resonances, and dispersive phenomena can be simultaneously displayed and readily identified. Since most antenna structures contain widely different in-band and out-of-band scattering characteristics, as well as complex scattering mechanisms such as leaky interior modes, time-frequency processing can be much better suited than the traditional feature spaces for interpreting the structural scattering phenomenology. In this work the standard short-time Fourier transform (STFT) is used to generate the time-frequency display.

Two geometries are analyzed in this work: a finite waveguide with one slot on each end and a linear slotted waveguide array comprised of 16 equally spaced slots. It should be pointed out that other finite periodic structures such as dielectric and conducting strip gratings have been analyzed previously in [8] and [11], showing that time-frequency processing can result in very good insights into all the phenomena involved. In addition, the use of time-frequency processing to antenna measurement data has been reported by Kent *et al.* [10]. As we shall show in this work, the time-frequency display of our simulated results reveals the different scattering physics involved. This makes it possible to pinpoint the various mechanisms, including both the Floquet harmonics due to the exterior slot structure and the interior waveguide modes.
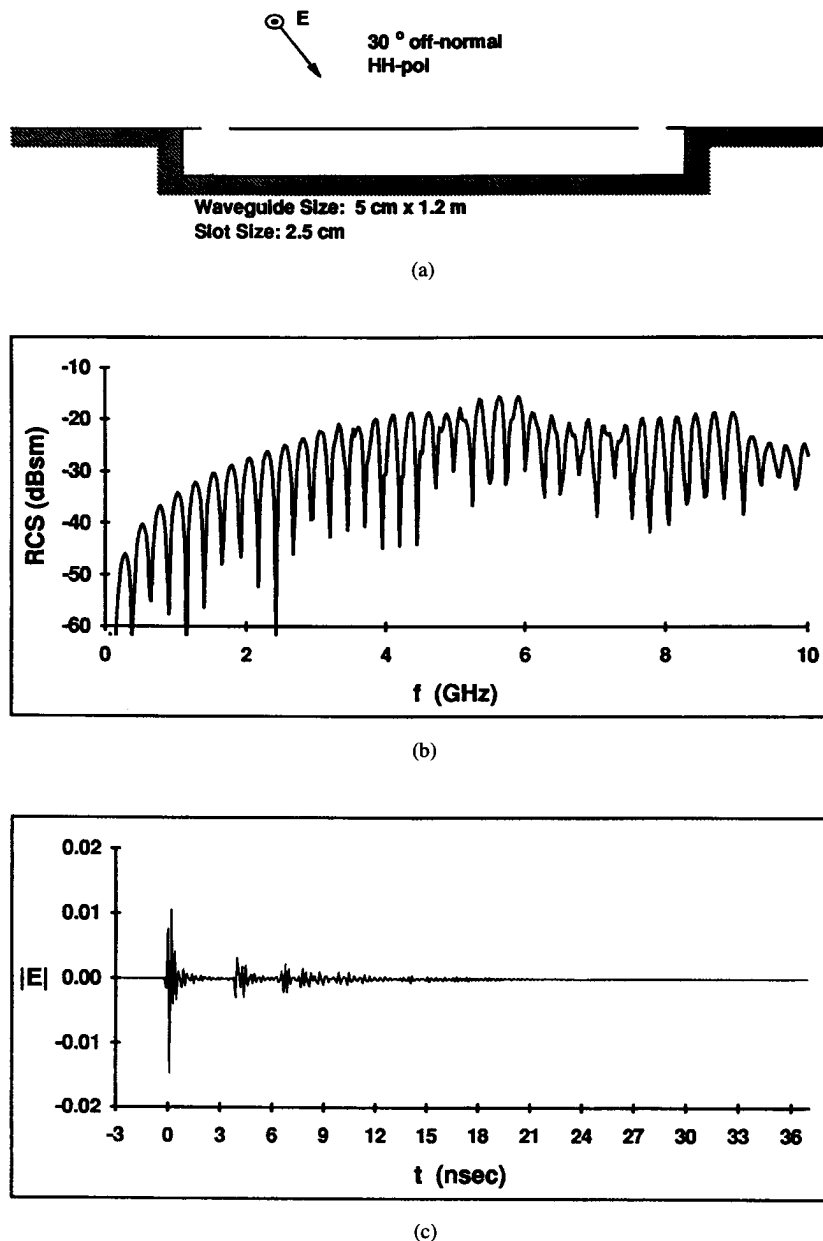
Fig. 1. Geometry of the 2-D slotted waveguide with two slots and its (a) computed, (b) frequency domain, and (c) time-domain backscattering.

II. SIMULATION AND PROCESSING OF SLOTTED WAVEGUIDE DATA

The two types of slotted waveguide structures studied are assumed to be flush mounted in an infinite conducting ground plane. The scattering data are numerically simulated by the application of the method of moments procedure as follows. We divide the structure into an inside and an outside region having the slots as the common boundary. The electric field tangent to the slot apertures is the assumed unknown, and a magnetic field integral equation is formulated by enforcing the continuity of the tangential component of the magnetic field. By applying the standard network formulation [14] in conjunction with the moment method procedure, we obtain a matrix equation of the form

$$\{[Y_{in}] + [Y_{out}]\}[V] = [I]. \tag{1}$$

In this equation $[I]$ is the incident magnetic field over the aperture, $[V]$ is the unknown electric field, and $[Y_{in}]$ and $[Y_{out}]$ are the generalized admittance matrices of the interior waveguide and of the half-space, respectively. The computation of $[Y_{out}]$ involves only the outside region and can be found easily by applying the equivalence principle and the method of images. The computation of $[Y_{in}]$ for an arbitrary interior structure, on the other hand, involves the discretization of the magnetic field on the interior waveguide walls and therefore would demand a large amount of computational resources as the length of the waveguide to be analyzed reaches 32λ at 10 GHz.

To reduce these requirements, a connection scheme [1], [2] based on the microwave network concept is used. We first divide the waveguide into a number of identical sections. By doing so, only a single section needs to be analyzed. For this section we obtain a generalized admittance matrix relating the
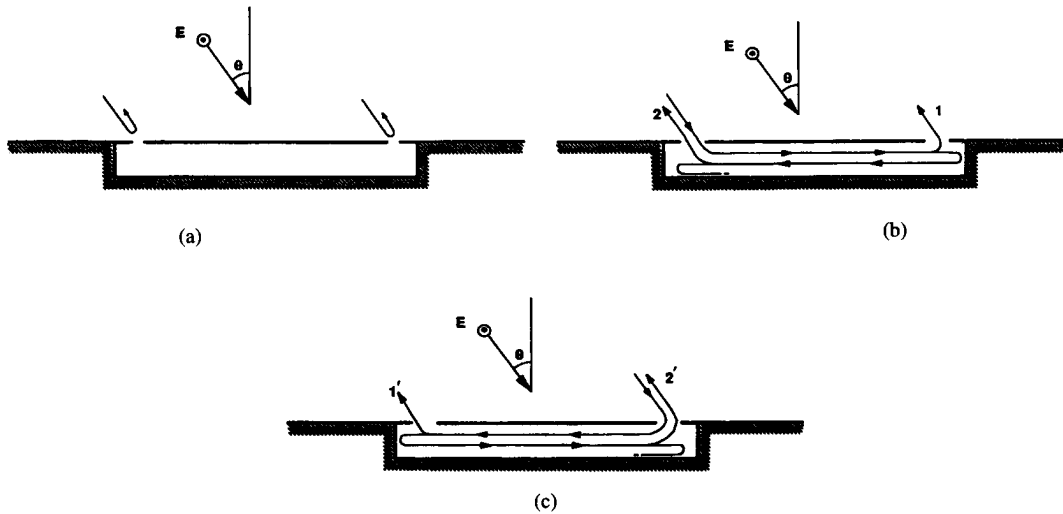
Fig. 2. Scattering mechanism interpretation of the waveguide with two slots, based on time-frequency display.
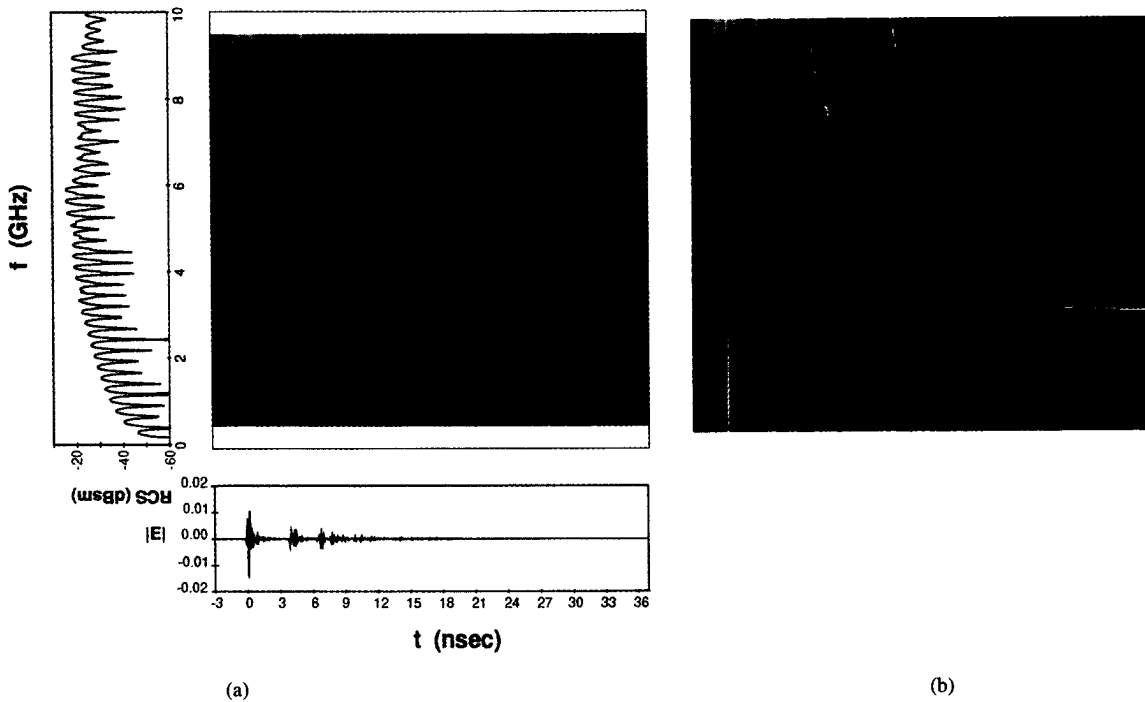

Fig. 3. (a) Time-frequency representation of backscattered data from the 2-D waveguide with two slots. (b) Comparison with predicted behavior.

electric and magnetic fields on its three apertures: the slot on the top and the two interfaces with adjacent sections on the two sides. The identical sections are then connected two-by-two by imposing the appropriate continuity conditions at the common boundaries to obtain the final admittance matrix $[Y_{in}]$ that relates the electric and magnetic fields on the slots only. This connection scheme, as explained in [1], leads to a drastic reduction in computational resources since the dimensions of the matrices that need to be stored and inverted become much smaller. For the discretization, triangular patch basis functions [15] are used along with Galerkin's testing. This procedure is described in more detail in [2].

The data obtained in the frequency domain are then processed using the inverse discrete Fourier transform (DFT) to generate the time-domain response. To better understand the phenomena involved, the STFT is also applied to the signal to obtain the time-frequency plots. The STFT is performed in the frequency domain using a Kaiser window with a bandwidth of 1 GHz. This window is shifted from a center frequency of 0.5 GHz up to 9.5 GHz, and the resulting windowed data are processed by the inverse DFT, generating each frequency row of the 2–D time-frequency plots shown in the next two sections.

III. TIME-FREQUENCY INTERPRETATION OF A TWO-SLOT WAVEGUIDE

To acquire better insights into the phenomena involved with the scattering from a long finite waveguide with two slots, a 2–D simulation is first carried out. The geometry analyzed is shown in Fig. 1(a) where a 1.2 m long parallel plate waveguide

with height 5 cm is embedded in the ground plane. Two 2.5 cm slots are opened on each end of the ground plane. The structure is excited by the incidence of an E-polarized plane wave at an angle of 30 degrees with respect to the normal. The frequency sweep, shown in Fig. 1(b), is obtained by a 2-D moment method code. The data are generated from 25 MHz to 10 GHz in 25 MHz increments.

From the time-domain data shown in Fig. 1(c), we see the signal scattered by the two slots at $t = 0$ and at $t = 3.75$ nsec, as expected. This phenomenon is illustrated in Fig. 2(a). The delay between the two pulses is given by $2L\sin\theta/c$, where $L = 112.5$ cm is the distance between the slots and c is the speed of light. We also notice that there are some other scattering mechanisms taking place after 3.75 nsec. A better way to interpret these mechanisms is by the time-frequency representation of the data, as shown in Fig. 3(a). The two early-time vertical lines correspond to the exterior scattering centers from the slots as described above. The other curves, which are dispersive ones, are related to signals coupled into the waveguide. These phenomena are depicted in Fig. 2(b). When the wave reaches the first slot some energy is coupled into the waveguide, propagating to the other end as a sum of waveguide modes. These modes will start to reradiate through the other slot after a time given by L/c, and the total delay will then be given by $(L + L\sin\theta)/c$ which is equal to 5.625 nsec. This mechanism is indicated by the mechanism labeled "1" in Fig. 2(b). That is the delay only for frequencies well above the cutoff, however, for which the group velocity approaches c. For frequencies approaching the cutoff frequency of the respective mode, the group velocity tends to zero and the delay goes to infinity. This behavior can be seen clearly in Fig. 3(a) where we observe the presence of two modal dispersion curves with cutoffs at 3 GHz and at 6 GHz ($f_c = nc/2a, a = 5$ cm, $n = 1, 2$). The equations for these curves in the time-frequency plane can be easily derived by considering the wave propagation inside the waveguide. After propagating a distance L inside the waveguide, the phase delay of a signal carried by mode n is given by

$$\Phi = 2\pi\sqrt{f^2 - f_{c,n}^2}\,\tau, \quad \tau = L/c \qquad (2)$$

where $f_{c,n}$ is the cutoff frequency of the nth mode. Therefore, the group delay of this signal, t_g, can be written as

$$t_g = \frac{1}{2\pi}\frac{d\Phi}{df} = \frac{\tau f}{\sqrt{f^2 - f_{c,n}^2}}. \qquad (3)$$

t_g versus f describes the trace of the dispersion curve for mode n in the time-frequency plane. Of course the delay due to the propagation outside the waveguide (nondispersive) must be added to the above expression to find the proper turn-on time of the signal in the time-frequency plane. For example, an extra delay of $L\sin\theta/c$ is needed for the signal entering through the left slot and coming out through the right slot. The amplitude variation of the signal along this curve, on the
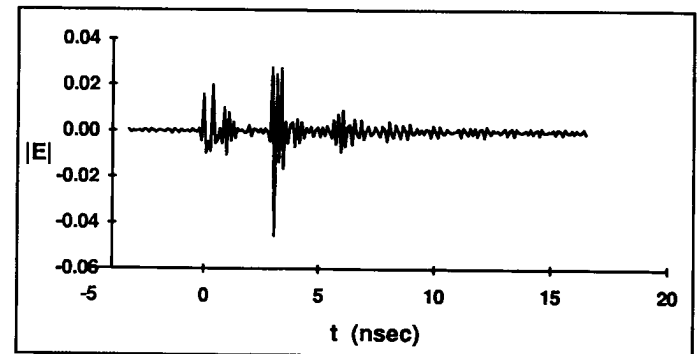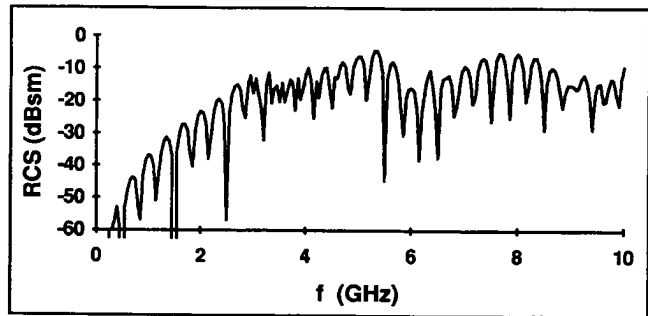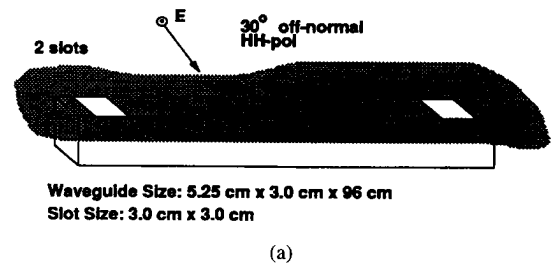
other hand, is governed by the coupling mechanisms through the slot apertures and is considerably more complex.

Since multiple reflections occur, we also see other dispersion curves with greater delays (7.5, 11.25, 13.125, $\cdots$ nsec) during the late-time (due to greater values of τ). The first one, which occurs after a delay of 7.5 nsec, corresponds to the energy that upon reaching the other end reflects back and radiates through the slot on the left, as indicated by the mechanism labeled "2" in Fig. 2(b). The three-bounce mechanism has a delay of 13.125 nsec. Note that energy is also coupled into the waveguide through the slot on the right, and through similar mechanisms generate dispersion curves in the time-frequency plot with delays of 5.625, 11.25, 13.125, $\cdots$ nsec, depending on the number of bounces. These mechanisms are illustrated in Fig 2(c). Finally, we should point out that the time-frequency characteristics for this structure are very similar to those found

Waveguide Size: 5.25 cm x 3.0 cm x 96 cm
Slot Size: 3.0 cm x 3.0 cm

(a)

(b)

(c)

Fig. 4. Geometry of the 3-D slotted waveguide with two slots and its (a) computed frequency, (b) time, and (c) backscattering.
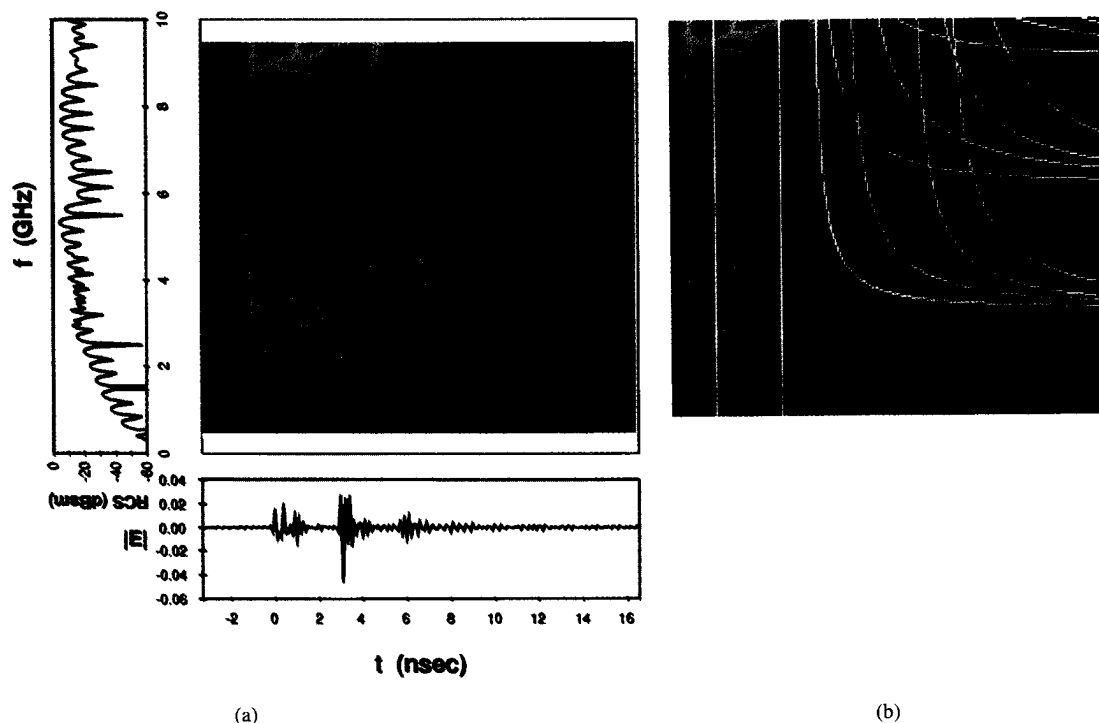
Fig. 5. (a) Time-frequency representation of backscattered data from the 3-D waveguide with two slots. (b) Comparison with predicted behavior.

for the open-ended waveguide duct analyzed in [3] and [4]. In that case, however, since most of the energy was radiated after the first reflection from the end of the duct, we could see only one dispersion curve for each mode propagating in the waveguide.

In Fig. 3(b) we plotted the expected time-frequency behavior, based on (2) and (3) and the above interpretation, on top of the STFT display of the signal. We see that the results obtained fully support our physical interpretation of the phenomena involved.

For a three-dimensional (3-D) structure shown in Fig. 4(a) which has a length of 96 cm (32λ at 10 GHz) and a cross section of 5.25 cm × 3.0 cm with two slots of dimensions 3.0 cm × 3.0 cm on the two ends of the narrow waveguide wall, we proceed in the same manner as the 2-D case. The incident polarization is horizontal with respect to the ground plane. The frequency domain data in Fig. 4(b) are generated from 50 MHz to 10 GHz in 50 MHz increments. The computation time is approximately 20 minutes per frequency, using 5.3 unknowns per squared centimeter, on a Silicon Graphics Indigo workstation (R4000 CPU). The time-domain data shown in Fig. 4(c) are obtained by the inverse DFT. The same comments regarding the exterior scattering at the two slots apply here. We notice more ringing in the time response, however, due to the resonance of the slots themselves.

In the time-frequency display of Fig. 5(a), we can again identify the exterior scattering from the slots as the two vertical lines. We notice the presence of two high-intensity (red) spots on each vertical line around 5.5 and 8 GHz, corresponding to the resonance of the slot apertures. We also see dispersive curves similar to those in the 2-D case. In this case the cutoff frequencies of the modes excited are at 2.86, 5.71, and

8.57 GHz which correspond to the modes TE_{10}, TE_{20}, and TE_{30}. Due to the symmetry of the structure and the incident excitation, neither TM modes nor $TE_{m,(2k+1)}$ modes can be excited. No TM modes can be excited because there is no component of the electric field normal to the cross section of the waveguide. No $TE_{m,(2k+1)}$ modes can be excited due to the even symmetry of the incident field along the narrow wall of the waveguide.

In Fig. 5(b) we show a comparison between the STFT display and the expected behavior for this geometry based upon (2) and (3). Again the agreement is reasonable. Of course in this case the image is somewhat more blurry in comparison with the 2-D results. This could be due to a stronger frequency dependence of the energy coupling through the slots for the 3-D case. In addition, the coarser frequency discretization used in the 3-D simulation leads to some aliasing. We also do not rule out possible computational noise in the much more involved 3-D simulation.

IV. TIME-FREQUENCY INTERPRETATION OF A 16-SLOT WAVEGUIDE ARRAY

The geometry of the 16-element slotted waveguide array is shown in Fig. 6(a). The waveguide is 96 cm long with cross section dimensions of 5.25 cm × 4.5 cm. It is flush mounted under an infinite conducting plane and has 16 equidistant slots of dimensions 4.5 cm × 1.5 cm on its narrow wall. The structure is excited by the incidence of a horizontally polarized plane wave at an angle of 30 degrees with respect to the normal. The frequency domain data shown in Fig. 6(b) are obtained from 2–10 GHz in 50 MHz increments, and the time-domain data in Fig. 6(c) are generated by the inverse DFT. The

Waveguide Size: 5.25 cm x 4.5 cm x 96 cm
Slot Size: 4.5 cm x 1.5 cm
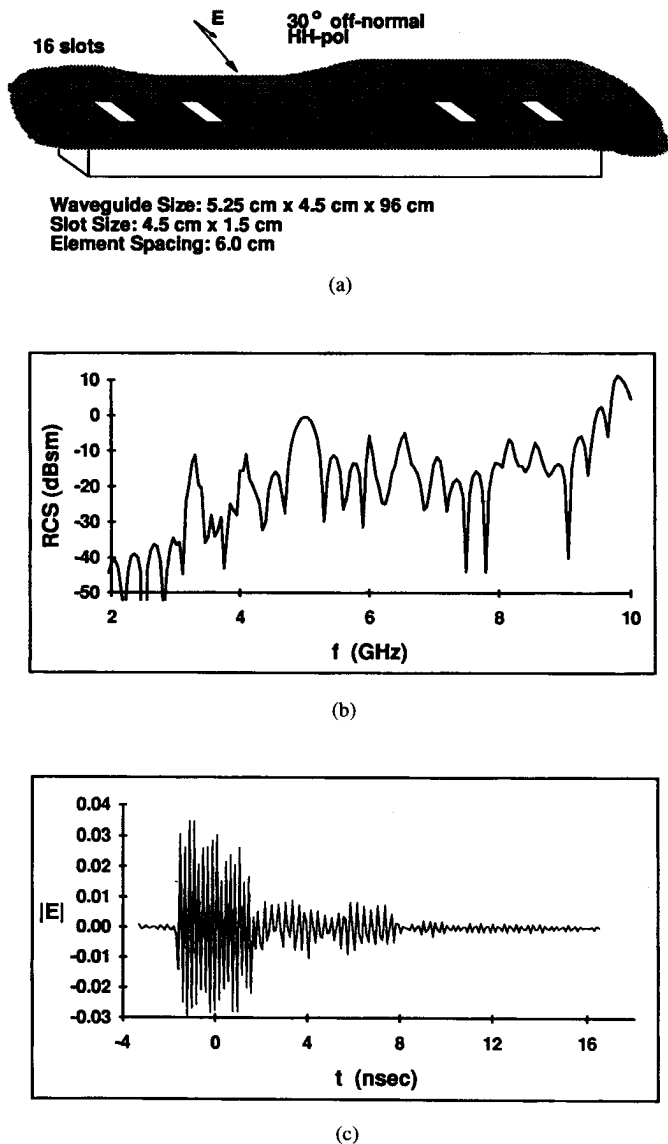**Element Spacing: 6.0 cm**

(a)

(b)

(c)

Fig. 6. Geometry of the 3-D slotted waveguide with 16 slots and its (a) computed frequency, (b) time, and (c) backscattering.

time origin in this graph was chosen to be the instant the wave reaches the middle of the structure.

From the time-domain response in Fig. 6(c), we observe the presence of 16 pulses between the time interval from -1.6 to 1.6 nsec. These distinct pulses correspond to the exterior scattering from the 16 slots in the structure. Due to the periodicity of the slots, the backscattered signals from each slot will reinforce each other at the discrete Floquet frequencies of

$$f = \frac{nc}{2d \sin \theta}. \tag{4}$$

Fig. 7(a) shows that the signal scattered by each slot has to propagate a distance equal to $2d \sin \theta$ longer than the previous one, and therefore the contribution of all the slots will add up when this length is equal to an integer multiple of the wavelength. For the array structure under consideration ($d = 6$ cm, $\theta = 30$ degrees), these angular-dependent Floquet resonances occur at 5, 10, 15, ... GHz. By examining the frequency plot in Fig. 6(b), we indeed see a major lobe at

TABLE I
FLOQUET FREQUENCIES OF ORDER p CORRESPONDING TO THE TE_{mn} MODE

m	n	p	f (GHz)
1	0	0	3.30
1	0	1	4.11
1	0	2	7.07
2	0	0	6.60
2	0	1	6.05
2	0	2	8.21
1	2	0	8.38
1	2	1	7.37
1	2	2	9.08
3	0	1	8.60
2	2	1	8.80

5 GHz. This peak is broad and has many sidelobes because the array structure is finite. The next Floquet resonance (or grating lobe in the array antenna terminology) can also be seen at slightly below 10 GHz. Besides these two Floquet frequencies, there are many other peaks in the frequency response which can be more easily identified in the time-frequency plane.

Fig. 8(a) shows the time-frequency display of the total scattered signal. The Floquet peak at 5 GHz can be seen to exist only between -1.6 and 1.6 nsec. The two very faint vertical lines that can be seen above 2 GHz correspond to the "edge effect" from the two ends of the finite array. We also observe the presence of many other resonances that decay with time but extend far beyond 1.6 nsec. These Floquet resonances are related to the modes excited in the waveguide that propagate from one end to the other, decaying as they radiate through the slots. This mechanism can be more easily explained in Fig. 7(b). Each excited mode which propagates from left to right radiates a signal through every slot. These signals have different phases, each being delayed by $k_{z,mn}\, d$ radians with respect to the previous one. Also, it will have to propagate an additional distance $d\sin\theta$ to the observation direction θ. Hence the total delay is $k_{z,mnd} + k_0\, d\sin\theta$, and we should observe a resonance at the frequencies for which this delay is an integer multiple of 2π. The same occurs for the modes when propagating from right to left as shown in Fig. 7(c), except that the total delay is now $k_{z,mnd} - k_0\, d\sin\theta$, leading to a different set of frequencies. This "interior Floquet" phenomenon has previously been reported in the study of finite dielectric gratings [8].

For each propagating mode in the waveguide we can therefore find a set of associated Floquet frequencies governed by the following equation

$$k_{z,mn} \pm k_0\, d\sin\theta = 2\pi p$$

$$k_{z,mnd} = \sqrt{k_0^2 - (m\pi/a)^2 - (n\pi/b)^2}. \tag{5}$$

In this equation the integer p is the index of the Floquet mode associated with each waveguide mode specified by the indices m and n, and a and b are the cross-sectional dimensions of the waveguide.

For the given dimensions and at the backscattering angle of 30 degrees, the frequencies that satisfy (5) for the excited modes in the waveguide are given in Table I. Due to the symmetry of the structure and the nature of the excitation, neither TM modes nor $TE_{m,(2k+1)}$ modes are excited in the structure. Moreover m cannot be zero.
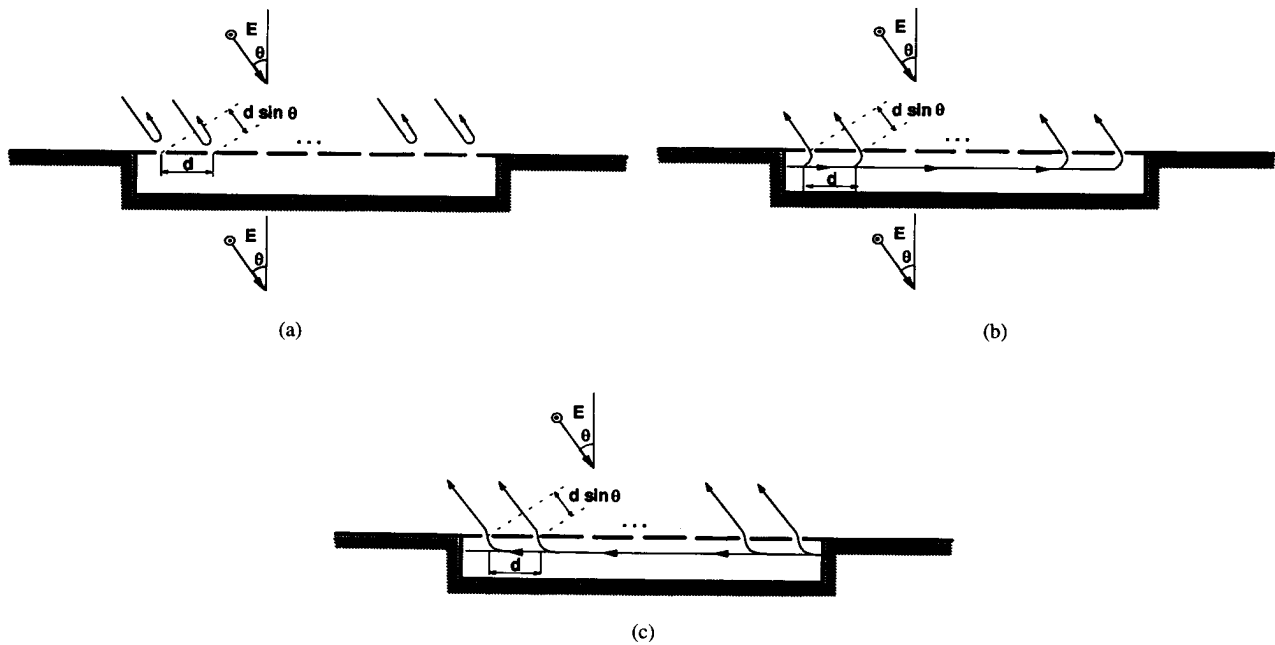
Fig. 7. Scattering mechanism interpretation of the waveguide with 16 slots, based on time-frequency display.
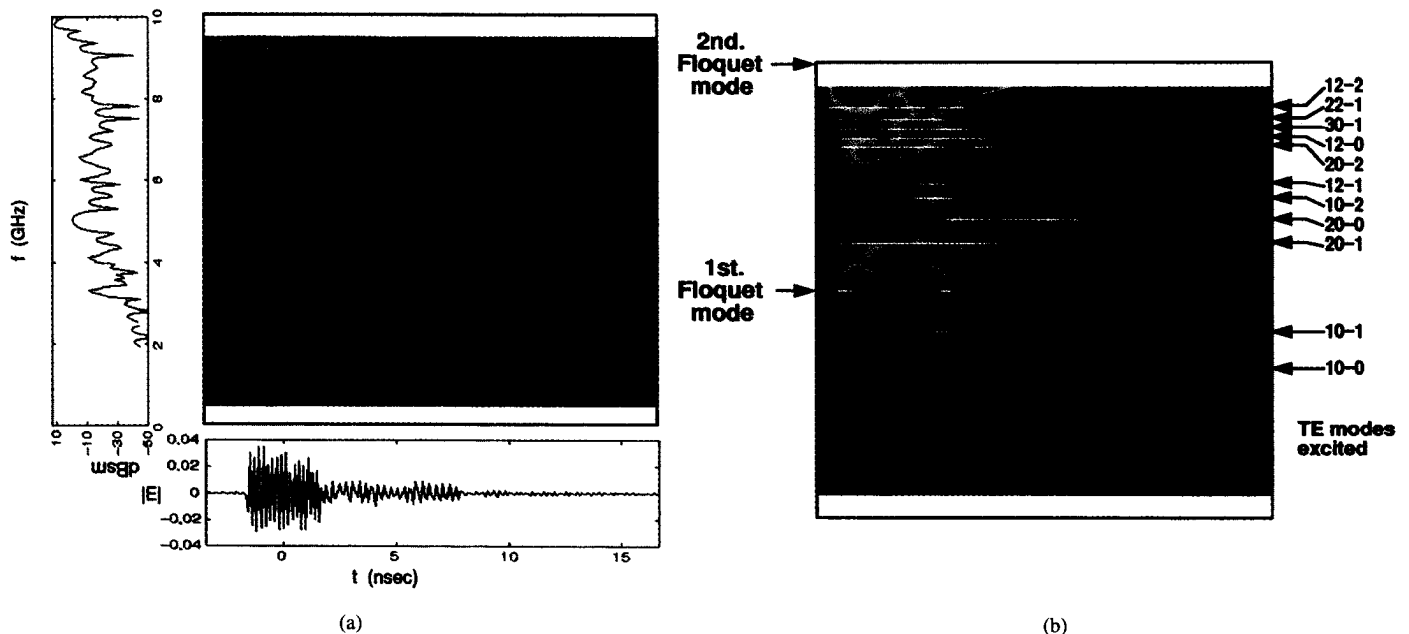

Fig. 8. (a) Time-frequency representation of backscattered data from the 3-D waveguide with 16 slots. (b) Floquet modes expected to be excited.

In Fig. 8(b) the positions of the calculated resonance frequencies from Table I are overlaid on the time-frequency plot. The first two digits correspond to the indices (m, n) of the waveguide mode, and the last digit is the index p of the associated Floquet mode (note that there are more than one Floquet mode associated with each waveguide mode). We observe that the agreement between the calculated resonances and the actual Floquet lines is reasonably good, considering the resolution limitations of the STFT, supporting the interpretation given above.

V. SUMMARY AND DISCUSSIONS

The scattering phenomenology in slotted waveguide structures has been investigated using time-frequency processing of numerically simulated data. An analysis of the mechanisms involved in the backscattering of two slotted waveguide structures has been presented. The dominant scattering mechanisms, related to the external scattering centers and the interior modes excited in the waveguide, could be well understood and visualized in the joint time-frequency plane with the application of the STFT.
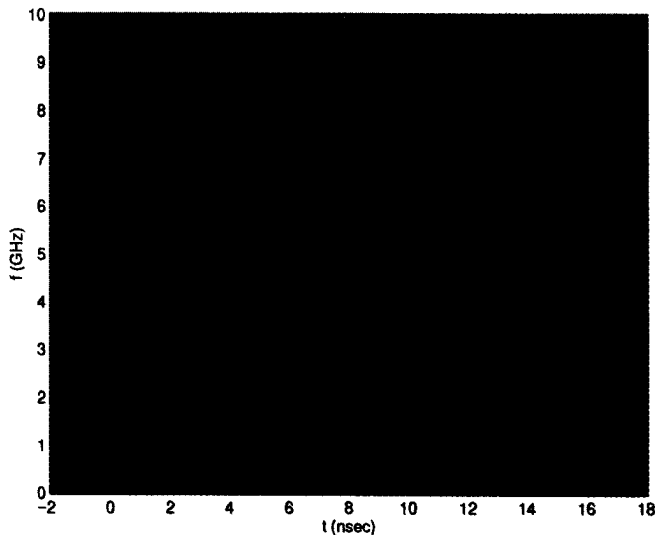
Fig. 9. Super-resolved time-frequency representation of backscattered data from the 3-D waveguide with two slots.

Fig. 10. Adaptive spectrogram of backscattered data from the 3-D waveguide with 16 slots.

It is well known that the STFT is limited in its resolution. As the target scattering phenomenology grows in complexity, the resolution problem will become more severe. A number of techniques including the multiresolution wavelet transform [6], super-resolution techniques such as Prony's or ESPRIT algorithms [12], [16], [17], and the adaptive spectrogram [18], [19] can potentially be applied to overcome the resolution issue. They are currently being pursued. As an example, Fig. 9 shows a super-resolved time-frequency representation by applying a sliding window ESPRIT algorithm to the 3-D data with two slots. In comparison with Fig. 5, we observe that while the algorithm extracted the two scattering centers adequately, the dispersion curve extraction is far from satisfactory. Fig. 10 shows the time-frequency display of applying the adaptive spectrogram technique to the 3-D data with 16 slots. In comparison with Fig. 8, the algorithm resulted in a much better frequency resolution for the late-time resonances. The early-time interpretation, however, is quite ambiguous. As can be seen in these two examples, much work is still needed in the high-resolution time-frequency processing arena. The STFT, on the other hand, is very robust and reliable and will probably remain as a fundamental tool for analyzing data containing complex mechanisms.

Finally, the algorithms used in this study can be applied easily to more realistic slotted waveguide array antennas. The main difference between our examples and a more realistic waveguide array antenna is the presence of match loads and/or feed networks in the real array. These extra structures, however, will likely only impact the scattering behavior of the antenna over a narrow frequency band. Another feature not modeled in our study is the slanting of the slot elements for amplitude control. Again, this is not expected to significantly alter the conclusions reached in this study.

ACKNOWLEDGMENT
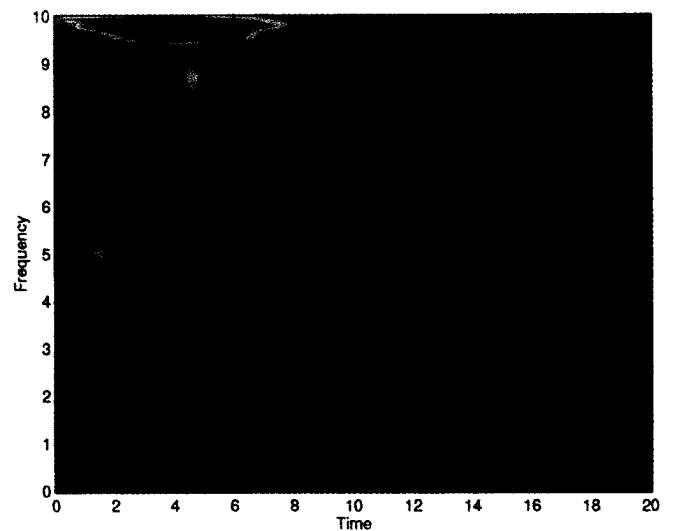
REFERENCES

[1] T. M. Wang and H. Ling, "Electromagnetic scattering from three-dimensional cavities via a connection scheme," *IEEE Trans. Antennas Propagat.*, vol. 39, pp. 1505–1513, Oct. 1991.

[2] L. C. Trintinalia and H. Ling, "Electromagnetic scattering from 3-D arbitrary coated cavities via a connection scheme using triangular patches," *J. Electromag. Waves Appl.*, vol. 8, pp. , Nov. 1994.

[3] A. Moghaddar and E. K. Walton, "Time-frequency distribution analysis of scattering from waveguide cavities," *IEEE Trans. Antennas Propagat.*, vol. 41, pp. 677–680, May 1993.

[4] H. Ling and H. Kim, "Wavelet analysis of backscattering data from an open-ended waveguide cavity," *IEEE Microwave Guided Wave Lett.*, vol. 2, pp. 140–142, Apr. 1992.

[5] H. Kim and H. Ling, "Wavelet analysis of electromagnetic backscatter data," *Elect. Lett.*, vol. 3, pp. 279–281, Jan. 1992.

[6] ———, "Wavelet analysis of radar echo from finite-size targets," *IEEE Trans. Antennas Propagat.*, vol. 41, pp. 200–207, Feb. 1993.

[7] H. Ling, J. Moore, D. Bouche, and V. Saavedra, "Time-frequency analysis of backscattered data from a coated strip with a gap," *IEEE Trans. Antennas Propagat.*, vol. 41, pp. 1147–1150, Aug. 1993.

[8] J. Moore and H. Ling, "Time-frequency analysis of the scattering phenomenology in finite dielectric gratings," *Microwave Opt. Tech. Lett.*, vol. 6, pp. 597–600, Aug. 1993.

[9] A. Moghaddar, E. K. Walton, and W. D. Burnside, "Time-frequency distribution of frequency-dispersive scattering using the wavelet transform," presented at the annual Non-Cooperative Target Identification Program Review, Air Force Wright Laboratory, Oct. 26, 1993.

[10] W. Kent, R. Layden, and J. Berrie, "Antenna scattering: Measurements and time-frequency," presented at the annual Non-Cooperative Target Identification Program Review, Air Force Wright Laboratory, Oct. 28, 1993.

[11] L. Carin, L. B. Felsen, D. Kralj, S. U. Pillai, and W. C. Lee, "Dispersive modes in the time domain: Analysis and time-frequency representation," *IEEE Microwave Guided Wave Lett.*, vol. 4, pp. 23–25, Jan. 1994.

[12] J. Moore and H. Ling, "Super-resolved time-frequency analysis of wideband backscattered data," *IEEE Trans. Antennas Propagat.*, vol. 43, no. 6, June 1995.

[13] H. Ling, J. Moore, H. Kim, L. C. Trintinalia, R. Bhalla, and G. Xu, "Time-frequency processing of wideband radar echo—From fixed resolution to multiresolution and super-resolution," in *Proc. Second Int. Conf. Ultra-Wideband, Short-Pulse Electromagnetics*, Brooklyn, NY, Apr. 1994.

[14] R. F. Harrington and J. R. Mautz, "A generalized network formulation for aperture problems," *IEEE Trans. Antennas Propagat.*, vol. AP-24, pp. 870–872, Nov. 1976.

[15] S. M. Rao, D. R. Wilton, and A. W. Glisson, "Electromagnetic scattering by surfaces of arbitrary shape," *IEEE Trans. Antennas Propagat.*, vol. AP-30, pp. 409–418, May 1982.

[16] J. Moore, L. C. Trintinalia, H. Ling, and G. Xu, "Super-resolved time-frequency processing of wideband radar echo using ESPRIT," *Microwave Opt. Tech. Lett.*, vol. 9, pp. 17–19, May 1995.

[17] L. C. Trintinalia and H. Ling, "Super-resolved parameterization of dispersive scattering mechanisms in the time-frequency plane," in *IEEE Antennas Propagat. Soc. Int. Symp. Dig.*, Newport Beach, CA, June 1995.

[18] S. Qian and D. Chen, "Signal representation using adaptive normalized Gaussian functions," *Signal Processing*, vol. 36, pp. 1–11, Mar. 1994.

[19] L. C. Trintinalia and H. Ling, "Time-frequency representation of wideband radar echo using adaptive normalized Gaussian functions," in *IEEE Antennas Propagat Soc. Int. Symp. Dig.*, Newport Beach, CA, June 1995.

Luiz C. Trintinalia was born in São Paulo, Brazil, on June 12, 1964. He received the B.S. degree in electrical engineering in 1987, and the M.S. degree, also in electrical engineering, in 1992, both from the Escola Politécnica da Universidade de São Paulo in Brazil. He is currently working on the Ph.D. degree in electrical engineering at the University of Texas in Austin.

He joined the faculty of the Escola Politácnica da Universidade de São Paulo in 1987 and is presently an Assistant Professor on leave from the Department of Electronic Engineering. His research interests include computational electromagnetics, radar signal processing, and target identification.

Hao Ling (S'83–M'86–SM'92) was born in Taichung, Taiwan, on September 26, 1959. He received the B.S. degrees in electrical engineering and physics from the Massachusetts Institute of Technology, Cambridge, in 1982, and the M.S. and Ph.D. degrees in electrical engineering from the University of Illinois at Urbana-Champaign, in 1983 and 1986, respectively.

He joined the faculty of the University of Texas at Austin in September 1986 and is currently a Professor of Electrical and Computer Engineering and holder of the Chevron Centennial Fellowship in Engineering. In 1982, he was associated with the IBM Thomas J. Watson Research Center, Yorktown Heights, NY, where he conducted low temperature experiments in the Josephson Program. While in graduate school at the University of Illinois, he held a research assistantship in the Electromagnetics Laboratory as well as a Schlumberger Fellowship. He participated in the Summer Visiting Faculty Program in 1987 at the Lawrence Livermore National Laboratory. In 1990, he was an Air Force Summer Fellow at the Rome Air Development Center, Hanscom Air Force Base. His research interests include radar signature prediction, computational techniques, and radar signal analysis for scattering mechanism interpretation and target identification.

Dr. Ling is a recipient of the National Science Foundation Presidential Young Investigator Award in 1987, the NASA Certificate of Appreciation in 1991, and the Archie Straiton, Junior Faculty Teaching Excellence Award in 1993.